

# Aggregation-Induced Dual Phosphorescence from (*o*-Bromophenyl)-Bis(2,6-Dimethylphenyl)Borane at Room Temperature

Zhu Wu,<sup>[a]</sup> Fabian Dinkelbach,<sup>[b]</sup> Florian Kerner,<sup>[a]</sup> Alexandra Friedrich,<sup>[a]</sup> Lei Ji,<sup>[a, c]</sup> Vladimir Stepanenko,<sup>[d]</sup> Frank Würthner,<sup>[d]</sup> Christel M. Marian,<sup>\*,[b]</sup> and Todd B. Marder<sup>\*,[a]</sup>

**Abstract:** Designing highly efficient purely organic phosphors at room temperature remains a challenge because of fast non-radiative processes and slow intersystem crossing (ISC) rates. The majority of them emit only single component phosphorescence. Herein, we have prepared 3 isomers (*o*, *m*, *p*-bromophenyl)-bis(2,6-dimethylphenyl)boranes. Among the 3 isomers (*o*-, *m*- and *p*-BrTAB) synthesized, the *ortho*-one is the only one which shows dual phosphorescence, with a short lifetime of 0.8 ms and a long lifetime of 234 ms in the

crystalline state at room temperature. Based on theoretical calculations and crystal structure analysis of *o*-BrTAB, the short lifetime component is ascribed to the  $T_1^M$  state of the monomer which emits the higher energy phosphorescence. The long-lived, lower energy phosphorescence emission is attributed to the  $T_1^A$  state of an aggregate, with multiple intermolecular interactions existing in crystalline *o*-BrTAB inhibiting nonradiative decay and stabilizing the triplet states efficiently.

## Introduction

Purely organic phosphors have received considerable research interest in optoelectronic devices,<sup>[1]</sup> bioimaging, molecular sensing,<sup>[3]</sup> and security printing,<sup>[4]</sup> due to efficient utilization of their triplet states. So far, most luminophores displaying room temperature phosphorescence (RTP) are restricted to inorganics containing noble transition metals such as iridium (Ir) and platinum (Pt), as transition-metal complexes are characterized by strong spin-orbit coupling (SOC) induced by heavy metal

ions and an intrinsic conformational rigidity which can theoretically harvest 100% of the electrically generated singlet and triplet excitons.<sup>[5]</sup> In addition, the phosphorescence emission spectra and quantum efficiencies can be tuned by modification of the ligand system. On the other hand, purely organic phosphors generally show inefficient intersystem crossing (ISC) and slow radiative decay rates from the lowest triplet state ( $T_1$ ) to the ground singlet state ( $S_0$ ).<sup>[6]</sup> In addition, the long-lived triplet excitons in metal-free luminophores can interact with environmental quenchers such as  $O_2$ , which quench the phosphorescence to a great extent.<sup>[7]</sup> In order to achieve RTP, one prerequisite is to enhance SOC to accelerate the ISC process, typically by utilizing heteroatoms, heavy atoms, or particular functional groups containing heteroatoms with lone pairs such as C=O, C=S or  $NR_2$ .<sup>[8]</sup> At the same time, it is also important to suppress nonradiative pathways and to isolate the chromophores from oxygen by host-guest doping,<sup>[9]</sup> crystallization,<sup>[10]</sup> or incorporation in a polymer matrix or on carbon dots.<sup>[11]</sup> Unlike trapped organic phosphors which emit only single component phosphorescence,<sup>[12]</sup> dual phosphorescence emission results from two different triplet states and was observed previously in a frozen glass matrix at low temperature.<sup>[13]</sup> More recently, dual room temperature phosphorescence (DRTP) in aggregated states was reported by several groups. For example, Tang's group developed a single-molecule white light phosphor which emits from both  $T_1$  and  $T_2$  states at room temperature.<sup>[14]</sup> Huang et al. reported a series of indole derivatives which show DRTP via inter-/intramolecular charge transfer.<sup>[15]</sup> Zhang et al. designed a number of D-*sp*<sup>3</sup>-linker-A-type triphenylamine (TPA) luminophores, which showed a TPA-localized triplet state  $T_1^L$  and an acceptor centered triplet state  $T_1^H$  simultaneously in a PMMA film.<sup>[16]</sup> Ma's group observed dual phosphorescence from pyridine-modified

[a] Dr. Z. Wu, Dr. F. Kerner, Dr. A. Friedrich, Prof. Dr. L. Ji, Prof. Dr. T. B. Marder  
Institut für Anorganische Chemie and  
Institute for Sustainable Chemistry & Catalysis with Boron  
Julius-Maximilians-Universität Würzburg  
Am Hubland, 97074 Würzburg (Germany)  
E-mail: todd.marder@uni-wuerzburg.de

[b] F. Dinkelbach, Prof. Dr. C. M. Marian  
Institut für Theoretische Chemie und Computerchemie  
Heinrich-Heine-Universität Düsseldorf  
Universitätsstr. 1, 40225 Düsseldorf (Germany)  
E-mail: Christel.Marian@hhu.de

[c] Prof. Dr. L. Ji  
Frontiers Science Center for Flexible Electronics (FSCFE) &  
Shaanxi Institute of Flexible Electronics (SIFE),  
Northwestern Polytechnical University  
Xi An Shi, 127 West Youyi Road, 710072 Xi'an (P. R. China)

[d] Dr. V. Stepanenko, Prof. Dr. F. Würthner  
Institut für Organische Chemie and Center for Nanosystems Chemistry  
Julius-Maximilians-Universität Würzburg  
Am Hubland, 97074 Würzburg (Germany)

Supporting information for this article is available on the WWW under  
<https://doi.org/10.1002/chem.202200525>

© 2022 The Authors. Chemistry - A European Journal published by Wiley-VCH GmbH. This is an open access article under the terms of the Creative Commons Attribution License, which permits use, distribution and reproduction in any medium, provided the original work is properly cited.

carbazole derivatives originating from  $T_1$  and  $T_1^*$  states.<sup>[17]</sup> Although several DRTP luminophores have been reported, research on this topic and the types of DRTP systems are still quite limited,<sup>[18]</sup> and there is no reliable design concept and strategy to achieve DRTP luminophores with high performance.

Based on our long standing interest in 3-coordinate organoboron materials and their optical and electronic properties,<sup>[19,20]</sup> we successfully designed persistent triarylborane phosphors with efficient ISC via  $(\sigma, B p) \rightarrow (\pi, B p)$  transitions.<sup>[21]</sup> However, it seemed likely that the SOC and, thus, the ISC rate constant could be improved. It is proposed that introducing heavy atoms (Br or I) into existing persistent RTP luminophores to enhance the SOC may greatly improve the performance of RTP phosphors. Br or I atoms can also provide multiple efficient intermolecular interactions to restrict nonradiative pathways, which is crucial to stabilize triplet states.<sup>[22]</sup> More importantly, the dense crystalline matrix provides a favorable environment for delocalization of the excitation and the formation of energy dispersed band structures.<sup>[23]</sup> Herein, we introduced the heavy atom Br into phenyl-bis(2,6-dimethylphenyl)borane at different positions on the phenyl ring to obtain 3 isomers (*o*-, *m*- and *p*-BrTAB, Figure 1c). Interestingly, (2-bromophenyl)bis(2,6-dimethylphenyl)borane (*o*-BrTAB) exhibits DRTP in the crystalline state under ambient conditions (Figure 1b). The faster, higher energy phosphorescence ranging from 430 to 490 nm with a short lifetime of 0.8 ms is ascribed to the  $T_1^M$  state of the monomer while the long-lived, lower energy phosphorescence emission in the range of 490–700 nm with a lifetime of up to 234 ms is attributed to the  $T_1^A$  state of an aggregate in the crystalline material.

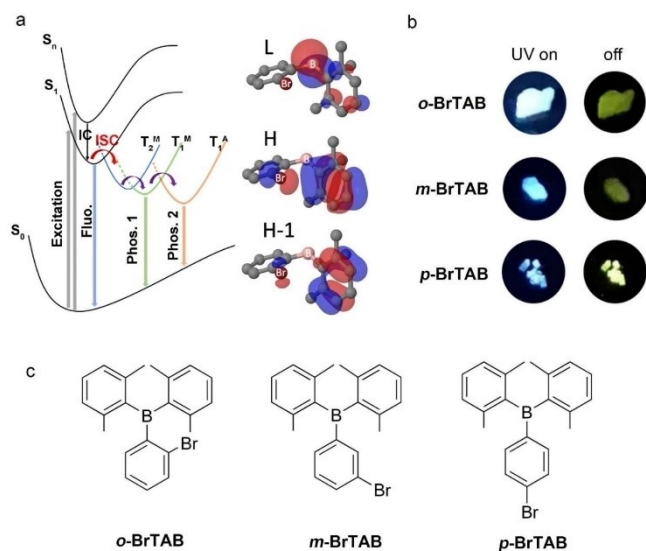


**Figure 1.** (a) Proposed mechanism of the dual phosphorescent emission in *o*-BrTAB and essential parts of the molecular orbitals involved in the transitions;  $T_1^M$  and  $T_1^A$  represent monomer states,  $T_1^A$  an aggregate state; (b) afterglow photographs taken before and after irradiation ( $\lambda_{\text{exc}} = 365$  nm) under ambient conditions; (c) molecular structures of the three isomeric compounds described in the paper.

## Results and Discussion

The compound *o*-BrTAB was synthesized<sup>[24]</sup> by reaction of the Grignard reagent (2,6-Me<sub>2</sub>-C<sub>6</sub>H<sub>3</sub>)MgBr with *o*-Br-C<sub>6</sub>H<sub>4</sub>BF<sub>3</sub>K, whereas *m*- and *p*-BrTAB were prepared by the reaction of bis(2,6-dimethylphenyl)fluoroborane with the respective aryl-lithium species generated by mono lithium-halogen exchange of *m*- or *p*-dibromobenzene with *n*-BuLi (for synthetic details and characterization data, see the Supporting Information). All three compounds showed absorption bands between 270 and 350 nm in hexane which are attributed to  $B \leftarrow \pi$  transitions with extinction coefficients of  $\epsilon = 10000\text{--}16000 \text{ M}^{-1}\text{cm}^{-1}$  (Figure 2a and Table 1). Placement of the Br atoms at the *ortho*, *meta* and *para* positions of the phenyl group had no obvious effect on the molecular energy levels of the three triarylboranes.

The spectra are composed of two absorption bands, where the lower energy band, around 300 nm, is more intense than the one at 260–270 nm. DFT/MRCI (multireference configuration interaction) calculations (Figure S10) show that the band at 300 nm is an overlay of the  $S_0 \rightarrow S_1$  and  $S_0 \rightarrow S_4$  absorptions, while the band at higher energy arises from the  $S_0 \rightarrow S_6$  absorption. They also reveal that irradiation of the compounds with UV light in the 310–320 nm wavelength regime predominantly populates the  $S_1$  state. The experimental fluorescence spectra of the 3 isomers in solution almost overlap, with emission maxima at 358 nm. Our calculations show the onsets of the fluorescence to occur at 348 nm for *o*-BrTAB, 328 nm for *m*-BrTAB and 324 nm for *p*-BrTAB, while experimentally, the onset is located at 328 nm for all three compounds. The computed fluorescence rate constants for *o*-, *m*-, and *p*-BrTAB are  $1 \times 10^7$ ,  $2 \times 10^7$  and  $2 \times 10^7 \text{ s}^{-1}$ , respectively, (Table S3) while their corresponding experimental fluorescence rate constants are  $1 \times 10^7$ ,  $6 \times 10^6$  and  $1 \times 10^7 \text{ s}^{-1}$ , respectively, showing good agreement between calculated and experimental values (Table 1 and Table S3).

We also measured the PL emission spectra in a frozen methylcyclohexane optical glass at 77 K (Figure 3). Compared to *m*- and *p*-BrTAB, which still show some residual fluorescence at higher energies (330–400 nm), only phosphorescence with a lifetime of 23 ms (57%) was observed in the spectrum of *o*-BrTAB, which indicates that ISC is very efficient and the phosphorescence quantum yield is much higher than that of fluorescence. Note that, as indicated in the footnote to Table 1, % values in parentheses are the contributions to a bi-exponential fit of the decays. Comparison of both experimental and computed fluorescence rate constants (ca.  $10^7 \text{ s}^{-1}$ ) with the fastest ISC rate constants for *o*-, *m*-, and *p*-BrTAB obtained from our theoretical calculations (see below) of  $1 \times 10^{10}$ ,  $9 \times 10^8$  and  $3 \times 10^8 \text{ s}^{-1}$  (Table S3), respectively, supports the above observations at 77 K in the frozen matrices. Thus, in the bromo-substituted triarylboranes, most of the excited state population is transferred to the triplet manifold, especially in *o*-BrTAB. The heavy atom effect of Br on the monomer phosphorescence radiative lifetimes is in the order *o*-BrTAB > *p*-BrTAB > *m*-BrTAB (Table S3), in agreement with the experimental trends listed in Table 1. The absence of DRTP in the frozen glass at 77 K suggests that the longer-lived phosphorescence component must originate from an aggregated state.

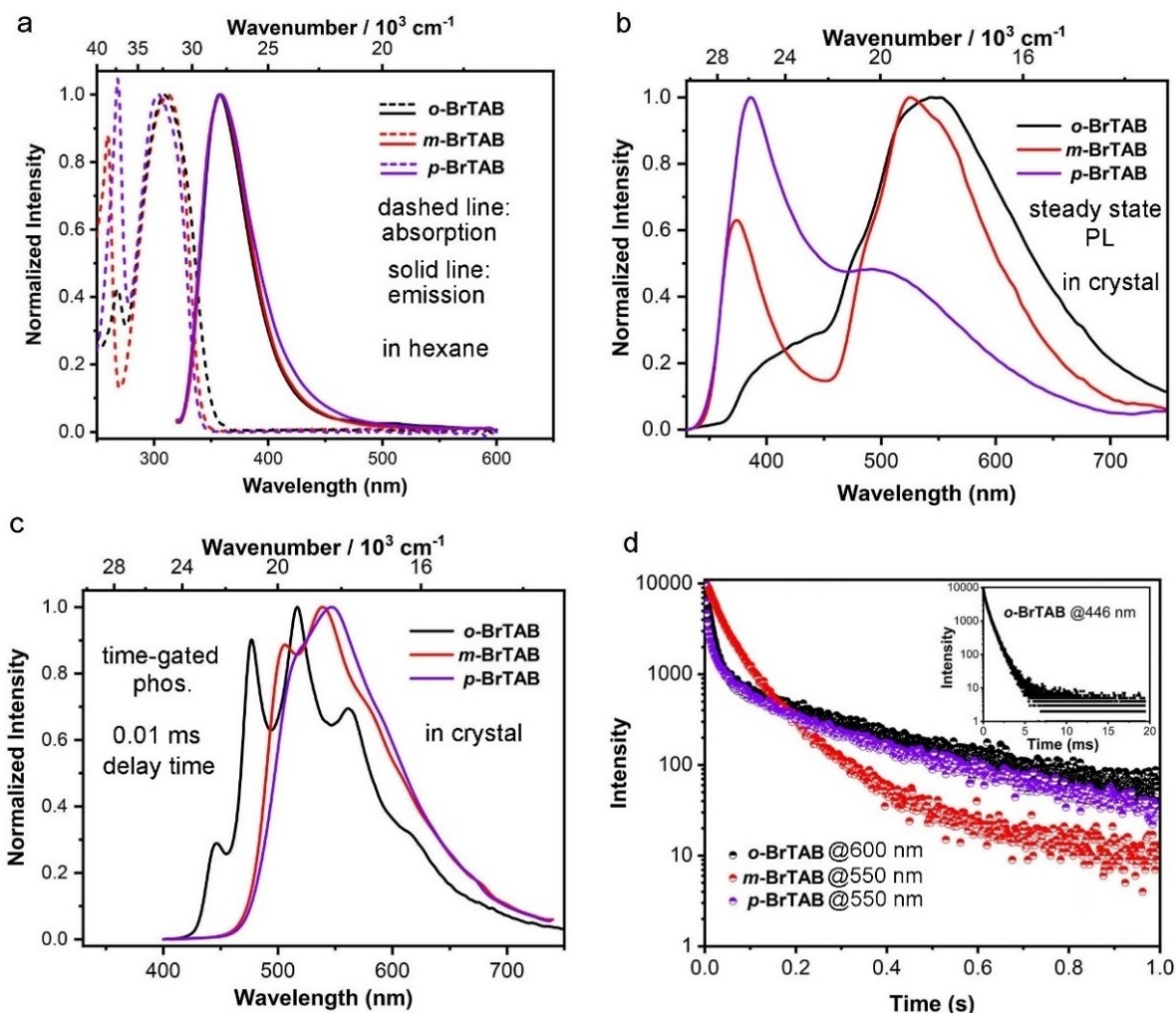


**Figure 2.** Normalized (a) UV/Vis absorption and fluorescence in hexane, (b) PL and (c) time-gated (0.01 ms delay) phosphorescence spectra of crystalline *o*-, *m*- and *p*-BrTAB ( $\lambda_{\text{ex}} = 305 \text{ nm}$ ). (d) Decays of the phosphorescence (600 nm for *o*-BrTAB and 550 nm for *m*- and *p*-BrTAB) in the crystalline state. Insert: decay of the phosphorescence (446 nm) of crystalline *o*-BrTAB. All above measurements were conducted at room temperature in air.

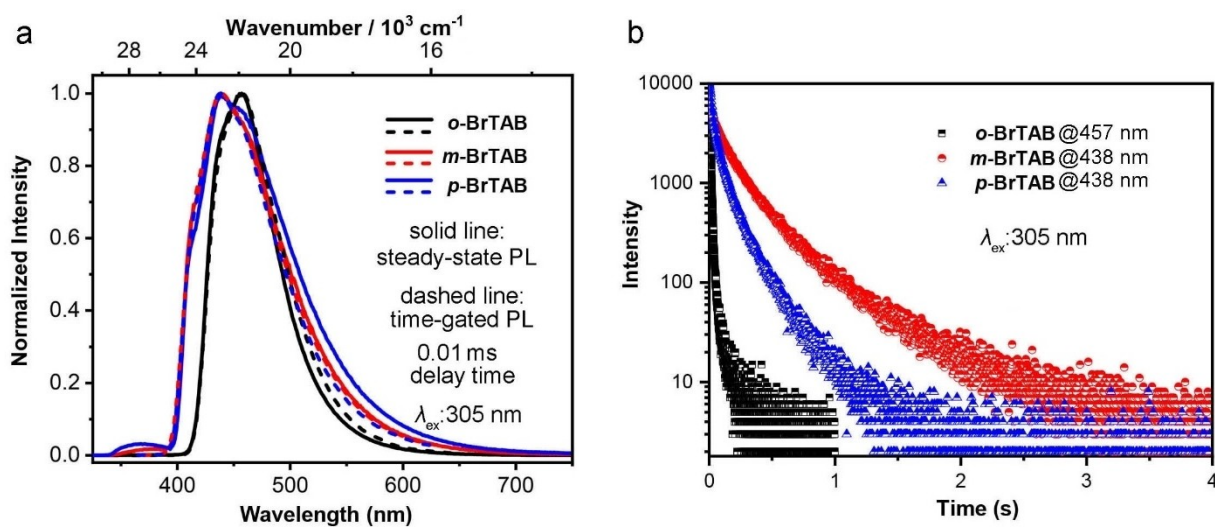


**Figure 3.** (a) Normalized photoluminescence (solid line) and time-gated phosphorescence (dashed line) spectra and (b) decays of the phosphorescence of *o*-, *m*- and *p*-BrTAB at their maximum emission wavelength in a frozen methylcyclohexane glass at 77 K ( $\lambda_{\text{ex}} = 305 \text{ nm}$ ).

**Table 1.** Photophysical properties of *o*-, *m*- and *p*-BrTAB in hexane and the crystalline state at RT, and in frozen methylcyclohexane and in the crystalline state at 77 K.

Compound	State [T]	$\lambda_{\text{abs}}$ [nm]	$E$ [ $\text{M}^{-1}\text{cm}^{-1}$ ]	$\Phi_{\text{PL}}$ [%]	$\lambda_{\text{f}}$ [nm]	$\Phi_{\text{f}}$ [%]	$\tau_{\text{f}}$ ns	$\tau_{\text{0}}^{\text{f}}$ [ns]	$k_{\text{r}}^{\text{f}}$ [ $\text{s}^{-1}$ ]	$\lambda_{\text{p}}$ [nm]	$\Phi_{\text{p}}$ [%]	$\tau_{\text{p}}$ ( $\text{T}_1^{\text{M}}$ ) [ms]	$\tau_{\text{p}}$ ( $\text{T}_1^{\text{A}}$ ) [ms]
<b><i>o</i>-BrTAB</b>	Solution (RT) <sup>[a]</sup>	312	10900	3.5	358	3.5	2.8	80	$1 \times 10^7$	nd <sup>[b]</sup>	–	nd	nd
	Crystalline (RT) <sup>[c]</sup>	–	–	1.5	– <sup>[d]</sup>	0.2	3.2	$8 \times 10^3$	$1 \times 10^5$	446, 477, 517, 562 <sup>[e]</sup>	1.3	0.3 (34%), 0.8 (66%)	13 (22%), 234 (78%)
	Crystalline (77 K)	–	–	–	–	–	–	–	–	431, 455	–	0.3 (28%), 2.1 (72%)	161 (42%), 453 (58%)
	Frozen glass (77 K) <sup>[f]</sup>	–	–	–	–	–	–	–	–	457	–	23 (57%), 92 (43%)	–
<b><i>m</i>-BrTAB</b>	Solution (RT) <sup>[a]</sup>	310	11300	1.4	358	1.4	2.3	164	$6 \times 10^6$	nd	–	–	nd
	Crystalline (RT) <sup>[c]</sup>	–	–	3.8	374	0.7	6.0	$3 \times 10^3$	$3 \times 10^5$	506, 539	3.1	–	64 (67%), 215 (33%)
	Crystalline (77 K)	–	–	–	374	–	–	–	–	430, 458, 483, 510	–	51 (54%), 153 (45%)	45 (28%), 512 (72%)
	Frozen glass (77 K) <sup>[f]</sup>	–	–	–	–	–	–	–	–	438	–	154 (55%), 486 (45%)	–
<b><i>p</i>-BrTAB</b>	Solution (RT) <sup>[a]</sup>	304	15200	1.2	358	1.2	1.7	77	$1 \times 10^7$	nd	–	–	nd
	Crystalline (RT) <sup>[c]</sup>	–	–	4.4	386	2.4	2.9	121	$8 \times 10^6$	547	2.0	–	90 (30%), 378 (70%)
	Crystalline (77 K)	–	–	–	386	–	–	–	–	427, 458, 510	–	18 (69%), 59 (31%)	166 (19%), 581 (81%)
	Frozen glass (77 K) <sup>[f]</sup>	–	–	–	367	–	–	–	–	438	–	53 (48%), 201 (52%)	–

[a] Measured in hexane at room temperature (RT); [b] not detected (nd); [c] measured in the crystalline state at RT; [d] The maximum fluorescence emission wavelength of *o*-BrTAB is estimated to occur at ca. 400–405 nm, but cannot be more accurately determined due to the overlap of fluorescence and phosphorescence; [e] 446 and 477 nm are ascribed to  $\text{T}_1^{\text{M}}$  and 517 and 562 nm are ascribed to  $\text{T}_1^{\text{A}}$ ; [f] measured in frozen methylcyclohexane at 77 K. For the phosphorescence lifetimes, the value given in % in parentheses is the contribution to a bi-exponential fit of the decay.

Recently, Sarkar, Hendrickson et al. reported on the three isomeric *o*-, *m*-, and *p*-bromobenzaldehydes.<sup>[25]</sup> When Br is *ortho* to the aldehyde, SOC is greatly enhanced, consistent with our observations. Looking at Table S3, the heavy Br atom effect leads to efficient ISC for all three compounds. However, while the fluorescence rate constant has the same order of magnitude ( $10^7 \text{ s}^{-1}$ ) for all three isomers, the ISC rate constants decrease in the order *o*->*m*->*p*-BrTAB. For *p*-BrTAB and *m*-BrTAB, ISC is 15 and 45 times faster, respectively, than fluorescence, so that residual fluorescence might be expected from those 2 isomers. For *o*-BrTAB, however, ISC is 1000 times faster than

fluorescence, so nearly all excited molecules rapidly form triplet states. As can be seen in the difference densities in Figures S13–15, bromine is involved more strongly in the excitation the closer it is located to the boron center. Following El-Sayed's rule,<sup>[27]</sup> a change in orbital character is required for a fast ISC process. This orbital change is visible in all three isomers, but most dominant in the *o*-BrTAB compound, where the Br *p*-orbital changes its orientation moving from the  $\text{S}_1$  to the  $\text{T}_2$  state (Figure 4) causing the squared SOCME to increase markedly to  $18640 \text{ cm}^{-2}$ . Despite the similarity of the electron distributions in both states (Figure 4), even the  $\text{S}_1^{\text{M}}$  and  $\text{T}_1^{\text{M}}$

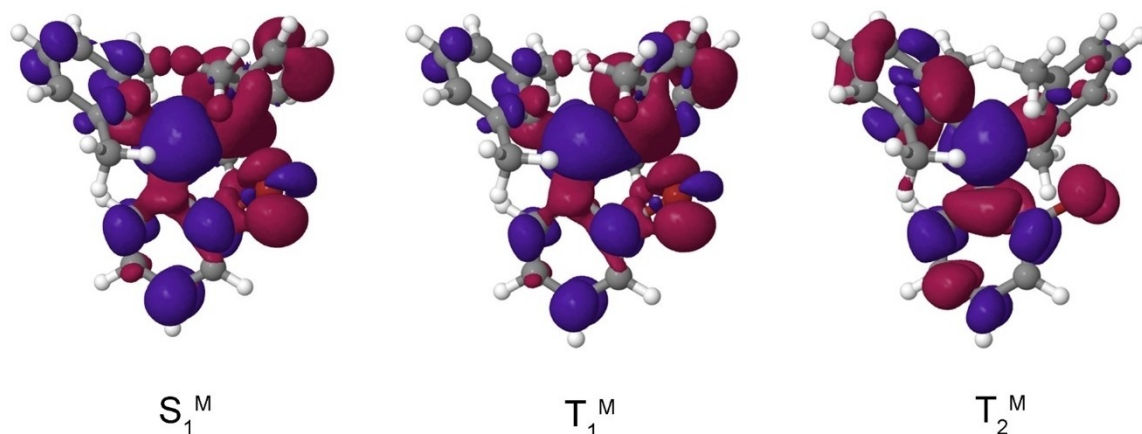


**Figure 4.** Difference of electron density distributions in the  $\text{S}_1^{\text{M}}$ ,  $\text{T}_1^{\text{M}}$  and  $\text{T}_2^{\text{M}}$  states of the *o*-BrTAB monomer with regard to the electronic ground state,  $\text{S}_0^{\text{M}}$ , at the  $\text{S}_1^{\text{M}}$  geometry. Red areas indicate a loss of electron density upon excitation, blue areas a gain. Note the reorientation of the *p* orbital hole on the bromine atom when proceeding from  $\text{S}_1^{\text{M}}$  to  $\text{T}_2^{\text{M}}$ .

states experience substantial mutual SOC in **o-BrTAB**. With a squared sum of SOCMs of  $25 \text{ cm}^{-2}$ , the  $S_1^M \rightarrow T_1^M$  transition is significantly faster ( $k_{ISC} = 2 \times 10^9 \text{ s}^{-1}$ ) than in the unsubstituted compound. Nevertheless, with a rate constant of ca.  $1 \times 10^{10} \text{ s}^{-1}$ , the  $S_1^M \rightarrow T_2^M$  ISC is five times faster than the direct  $S_1^M \rightarrow T_1^M$  ISC. Besides ISC, internal conversion (IC) plays an important role for the population of the emissive  $T_1$  state from higher triplet states. In **o-BrTAB** we found a conical intersection allowing a very efficient population transfer from  $T_2$  to  $T_1$  without the necessity to surmount a large energy barrier in the process.

In **m-BrTAB**, the largest SOCMs arise between the  $S_1^M \rightarrow T_2^M$  and  $S_1^M \rightarrow T_3^M$  pair of states. Both target states are similar in character except that the bromine involvement is more pronounced in the  $T_3^M$  state, yielding a rate constant of  $9 \times 10^8 \text{ s}^{-1}$  for the  $S_1^M \rightarrow T_3^M$  ISC in this isomer. In **p-BrTAB**, the bromine substitution primarily enhances the probabilities of the  $S_1^M \rightarrow T_1^M$  and  $S_1^M \rightarrow T_3^M$  ISCs. Here we find the  $T_2^M$  state to be more similar in character to the  $S_1^M$  state than the  $T_1^M$  state. The fastest ISC is found for the  $S_1^M \rightarrow T_3^M$  channel with  $k_{ISC} = 3 \times 10^8 \text{ s}^{-1}$ . A comparison of the ISC rate constants with the fluorescence rate constants of ca.  $10^7 \text{ s}^{-1}$  (Table S3) suggests that the fluorescence quantum yield is low and that most of the excited state population is transferred to the triplet manifold in the bromo-substituted triarylboranes, in particular in the **o-BrTAB** isomer, which is consistent with the low fluorescence intensities observed in a frozen glass at 77 K.

The phosphorescence rate constant of  $T_1$  depends essentially on three factors: the magnitude of the SOC matrix element (SOCME) between  $T_1$  and singlet states  $S_n$ , the energy difference between  $T_1$  and  $S_n$ , and the brightness of the  $S_n \rightarrow S_0$  transition. Interference effects aside, the larger the  $T_1$ - $S_n$  SOC, the smaller the  $T_1$ - $S_n$  energy difference, and the larger the  $S_n \rightarrow S_0$  transition dipole, the larger the phosphorescence probability.<sup>[26]</sup> Because of the large  $T_1$ - $S_2$  SOC and  $T_1$ - $S_4$  SOC, **o-BrTAB** can borrow substantial intensity from the spin-allowed bright transitions ( $S_2 \rightarrow S_0$  and  $S_4 \rightarrow S_0$ , respectively). In **m-BrTAB** and **p-BrTAB**, SOC between  $T_1$  and the low-lying singlet states is small and, therefore, the intensity borrowing is not very efficient. Hence, **o-BrTAB** is the only compound with a phosphorescence rate constant in the millisecond regime; the other two have rate constants of 5 s (**m-BrTAB**) and 1 s (**p-BrTAB**) according to the calculations.

However, the photoluminescence spectra at room temperature in the crystalline state are much different from the results in solution (Figure 2b). First, in addition to the fluorescence peaks attributed to the monomer excited state at short wavelength, broad peaks between 450 and 750 nm result from phosphorescence. The longer-lived (phosphorescence) emission lifetimes measured for **o-**, **m-** and **p-BrTAB** at room temperature are 234 (78%), 64 (67%) and 378 (70%) ms, respectively, where the percentages given are those of the larger component of a bi-exponential fit to the decay curves (Figure 2d). Second, the fluorescence emissions from crystalline samples of **o-**, **m-** and **p-BrTAB** are all redshifted compared with those in hexane solution. The bathochromic shift of **p-BrTAB** ( $2026 \text{ cm}^{-1}$ ) is approximately twice that of **m-BrTAB** ( $1194 \text{ cm}^{-1}$ ). Third, **o-BrTAB** has a larger ratio of phosphorescence to fluorescence

intensity, indicating that ISC in **o-BrTAB** is the most efficient of the three isomers. The time-gated phosphorescence spectrum of crystalline **o-BrTAB** at room temperature shows four fine structured bands at 446, 477, 517 and 562 nm, respectively (Figure 2c). The vibrational fine structure is also present in the computed Franck-Condon (FC) spectrum of the  $T_1^M$  emission, though less pronounced. We attribute it to a progression of a vibrational mode with a frequency of  $1673 \text{ cm}^{-1}$  in the electronic ground state which corresponds to an asymmetric C–C stretching motion of the xylyl ring closest to the Br atom.

The aggregation state of **o-BrTAB** has a large influence on the photoluminescence behavior. A ground solid sample of **o-BrTAB** exhibited multiple small size particles with increased surface area as observed by SEM (Figure S1). The powder X-ray diffraction pattern of the ground **o-BrTAB** sample shows its crystalline nature (Figure S3). In the ground sample, the exposed surface area is much larger than in the single crystal and, as slower phosphorescence is more sensitive to oxygen quenching, the ratio of phosphorescence to fluorescence dramatically decreased (Figure S2). The longer phosphorescence lifetime decreases significantly from 234 to 191 ms and the quantum yield is too small to be measured. The shorter phosphorescence lifetime also drops slightly to 0.7 ms, further indicating the important role of the aggregation state in the photoluminescence behavior. In addition, **o-BrTAB** was embedded in a poly(methyl methacrylate) (PMMA) matrix at different loading levels. In a highly doped film (40 wt%, Figure S4), the time-gated phosphorescence emission blueshifts (ca.  $600 \text{ cm}^{-1}$ ) compared to that in the crystalline state, and only the short lifetime (0.8 ms) component was detected, while in an even more concentrated PMMA film (60 wt%, Figure S5), the long lifetime (226 ms) component emerged. The experimental results clearly indicate that longer-lived component of the DRTP is induced by aggregation.

The DRTP was confirmed by time-gated phosphorescence spectroscopy of **o-BrTAB** at room temperature (Figure 5a). Upon increasing the delay time, the intensity of peaks of the shorter wavelength emission components at 446 and 477 nm decreased gradually. When the delay time was set at 3 ms, the short-lived monomer  $T_1^M$  emission of **o-BrTAB** almost disappeared, and the remaining long lifetime component is ascribed to phosphorescence from the  $T_1^A$  state of an aggregate. We performed time-gated excitation spectroscopy of crystalline **o-BrTAB** at 480 and 560 nm, respectively (Figures 5c and 5d). Upon increasing the delay time from 0.1 to 3 ms, the overall excitation intensity gradually decreases. We stress that the spectra at each delay time are identical in the range of 300 to 450 nm, indicating that one absorption leads to all excited states. We also measured time-gated phosphorescence spectra at different excitation wavelengths (Figure 5b). The two triplet excited states always appear at the same time which further indicates that  $T_1^M$  and  $T_1^A$  originate from the same absorption ( $S_0 \rightarrow S_1$  and  $S_0 \rightarrow S_n$ ). Furthermore, we measured the time-gated phosphorescence spectra of **o-BrTAB** in the crystalline state at different excitation wavelengths (300, 370 and 420 nm) and different delay times (0.1, 1.0, and 3.0 ms) (Figure 6). When a delay time of 0.1 ms was used to measure the time-gated

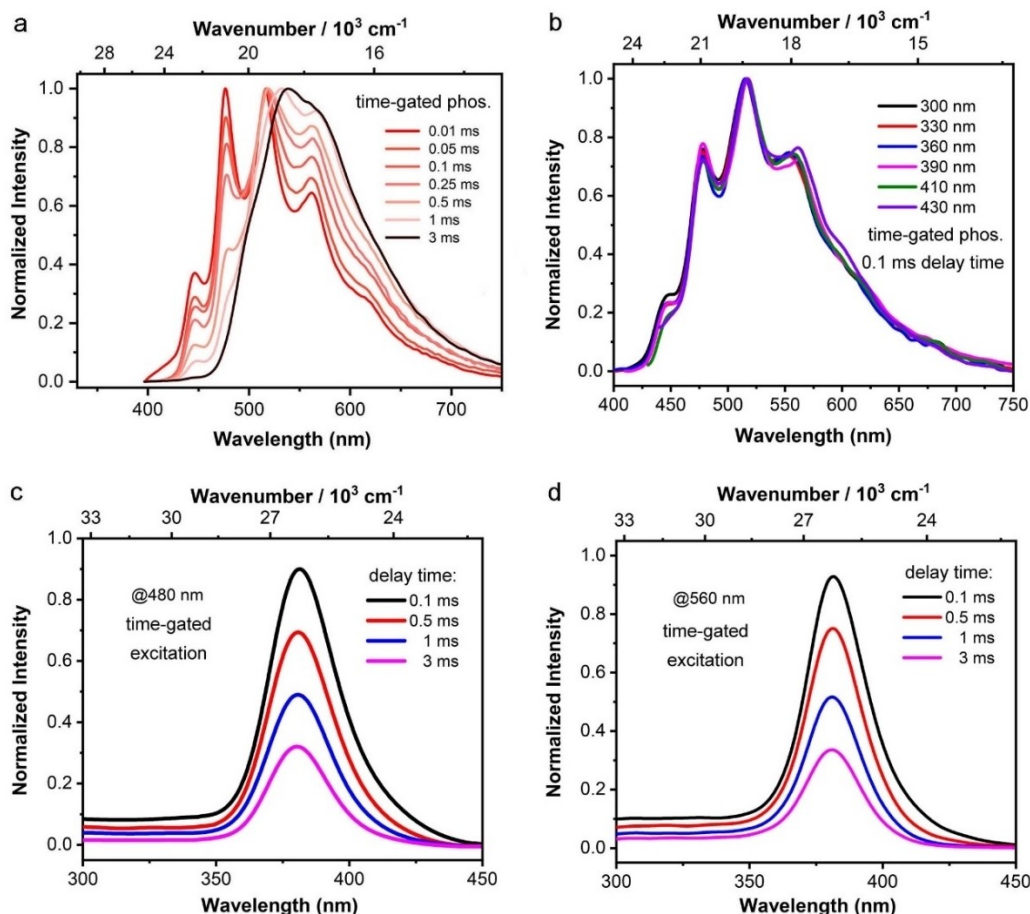


**Figure 5.** Normalized time-gated phosphorescence spectra of crystalline **o-BrTAB** (a) with different delay times and (b) with 0.1 ms delay at different excitation wavelengths. Time-gated excitation spectra (c,  $\lambda_{\text{em}} = 480$  nm) and (d,  $\lambda_{\text{em}} = 560$  nm) of crystalline **o-BrTAB** at different delay times at room temperature.

spectra of crystalline **o-BrTAB** at different excitation wavelengths (Figure 6a), the short-lived component  $T_1^M$  and long-lived component  $T_1^A$  are both apparent and the spectra at the three different excitation wavelengths are identical. When a longer delay time of 1.0 ms was used at different excitation wavelengths (Figure 6b),  $T_1^M$  and  $T_1^A$  also appear with a smaller relative intensity of the short-lived  $T_1^M$  component due to the time-gating effect. With a 3.0 ms delay time (Figure 6c), the relative intensity of the  $T_1^M$  component becomes even smaller, but it is still apparent. These results clearly indicate that the short-lived  $T_1^M$  and long-lived  $T_1^A$  components originate from the same absorption.

Therefore, we propose that first, the single molecule of **o-BrTAB** is excited into its  $S_1^M$  or  $S_n^M$  state. Then it undergoes ISC to  $T_2^M$  which undergoes IC to a short-lived  $T_1^M$  state. At the same time,  $T_1^M$  evolves into a  $T_1^A$  state, emitting more slowly and at lower energy. The process going from  $T_1^M$  to  $T_1^A$  was confirmed by temperature-dependent, time-gated spectroscopic study of crystalline **o-BrTAB** (Figure 7b). Upon decreasing the temperature from 298 to 77 K, the phosphorescence peaks belonging to  $T_1^M$  at 446 and 477 nm blueshift to ca. 431 and 455 nm, respectively, which become dominant at 77 K with a lifetime ca. 2.1 ms. At 77 K, the long-lived  $T_1^A$  emission at longer

wavelength still exists with a lifetime of ca. 453 ms (58%), but in a much lower ratio compared to the short-lived component. Thus, there is a thermal barrier for the conversion of  $T_1^M$  to  $T_1^A$ , and lowering the temperature makes it harder to cross the barrier.

For crystalline **m-** and **p-BrTAB**, we did not observe dual phosphorescence at room temperature, but only at low temperature. At 77 K, new emission peaks at 431 and 455 nm appeared in the time-gated spectra with the phosphorescence lifetimes of crystalline **m-** and **p-BrTAB** of 51 (54%) and 18 (69%) ms, respectively, being much shorter than the lifetimes 512 (72%) and 581 (81%) ms of the longer-wavelength emissions (Figures S6–S9). As the strength of intermolecular interactions is especially distinct between the three compounds at room temperature, only **o-BrTAB** exhibits strong intermolecular interactions, effectively suppressing the nonradiative decay rate  $k_{\text{nr}}$ , which plays an important role in stabilizing the triplet states. Hence, a nonradiative decay channel is opened for **m-** and **p-BrTAB** going from 77 K to RT. In **o-BrTAB**, the radiative channel can compete with the nonradiative one even at RT. This may be the reason that dual phosphorescence is only observed in **o-BrTAB** at room temperature and a detailed discussion of

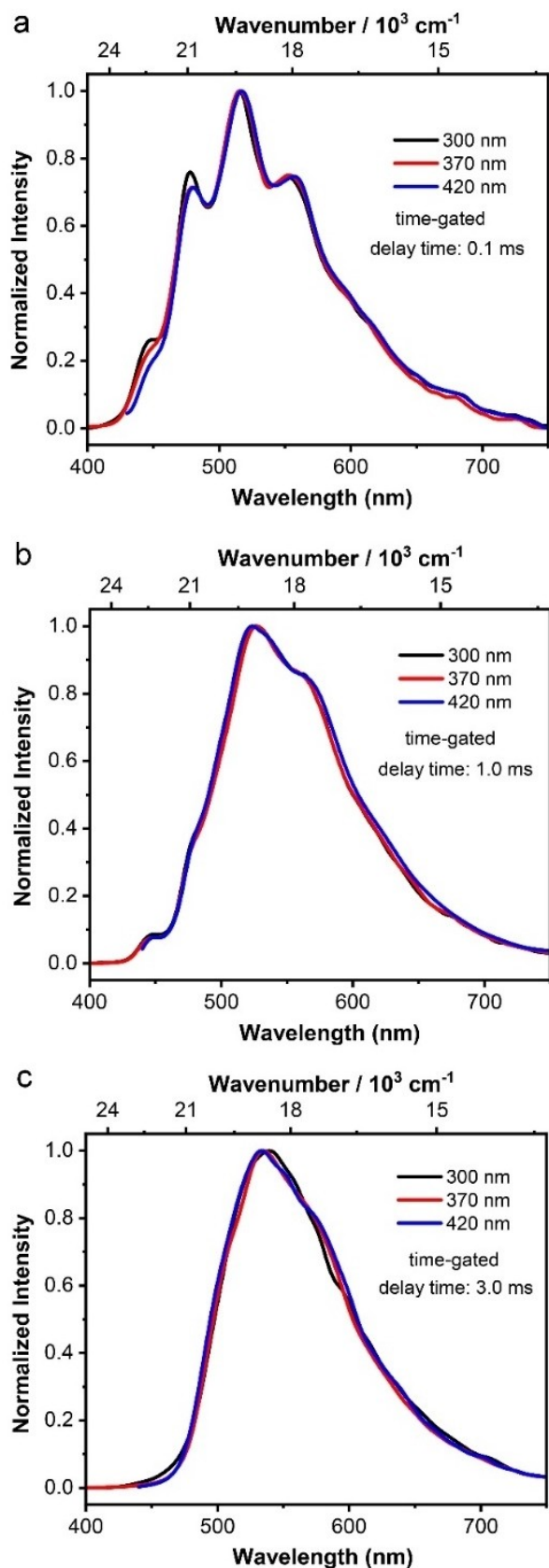


**Figure 6.** Normalized time-gated phosphorescence spectra of crystalline *o*-BrTAB at different excitation wavelengths ( $\lambda_{\text{ex}}$  = 300, 370 and 420 nm) and different delay times of (a) 0.1, (b) 1.0, and (c) 3.0 ms.

intermolecular interactions is provided in the crystal structure analysis section (see below).

To explain the experimentally observed dual phosphorescence, we first searched for the most probable pathways from the singlet to the triplet states of the monomer. For the unsubstituted compound phenyl-bis(2,6-dimethylphenyl)borane, we have already shown that the  $S_1 \rightarrow T_1$  transition is slower than  $S_1 \rightarrow T_2$ .<sup>[21]</sup> This can be rationalized by the stronger change in orbital character when moving from  $S_1$  to  $T_2$  and thus, following El-Sayed's rule,<sup>[27]</sup> the SOCMEs between  $S_1$  and  $T_2$  are much larger than those for  $S_1 \rightarrow T_1$ . The bromine substitution increases the SOCMEs in general with respect to those of the unsubstituted compound. As may be expected, the heavy-atom effect is strongest for the *ortho*-substituted compound. Even in this case, the change in excitation character is larger for the  $S_1^M \rightarrow T_2^M$  transition. In particular, the p orbital hole at the Br atom changes orientation (see above) as required for an El-Sayed allowed transition.<sup>[27]</sup> Very close to the  $T_2^M$  minimum, however, the  $T_2^M$  and  $T_1^M$  states of *o*-BrTAB undergo a conical intersection without the necessity to surmount a substantial energy barrier. Therefore, the population is not trapped in the  $T_2^M$  state but is rapidly transferred to the  $T_1^M$  state. The possibility that the dual phosphorescence originates from  $T_2^M$  and  $T_1^M$  states can be ruled out.

As dual phosphorescence was not observed from isolated molecules in the frozen glass matrix at 77 K but only in the crystalline state and in highly doped PMMA films, we propose that this phenomenon stems from aggregated *o*-BrTAB units. To explore this effect, we optimized dimeric systems of the compounds starting from the crystal structures. Spreading the excitation over a dimer is, unfortunately, not sufficient to cause a substantial stabilization of the excitonic state. Their difference densities (Figures S16-S18) reveal that the lowest excited dimer states are composed of excitations similar to those of the monomers. In the *o*-BrTAB dimer, the  $T_1^D$  state is stabilized by only 0.05 eV with respect to the monomer. Delocalization of the excitation over larger molecular clusters is required to explain the marked redshift of the long lifetime component of the phosphorescence emission in the crystalline state.

To understand the effect of the solid-state structures and the intermolecular packing on the luminescence properties, the structures of *o*-, *m*- and *p*-BrTAB were obtained at low temperature (100 K) and at ambient temperature (290 K for *o*-BrTAB, 296 K for *m*-BrTAB, and 300 K for *p*-BrTAB) using single-crystal X-ray diffraction (Figure 8). Comparison of the molecular geometries of *o*-, *m*- and *p*-BrTAB in their crystal structures shows only a small effect of the Br atom position on the bond lengths and angles. All but one of the B–C bond distances are similar within 3 esd's (1.574(3)–1.585(2) Å at 100 K). Only the B–C bond to the Br-substituted aryl ring in *p*-BrTAB is significantly shorter (1.563(2) and 1.561(2) Å for the two non-symmetry equivalent molecules at 100 K, Table S11). The  $BC_3$  moiety is planar in all three compounds with the sum of C–B–C angles being  $360^\circ$  within the standard uncertainties. The individual angles are in the range  $118.0(2)$ – $122.9(2)^\circ$  except for the C1–B–C7 angle in *o*-BrTAB which is significantly smaller ( $116.3(2)^\circ$  at 100 K, Table S11). This is the angle between the Br-

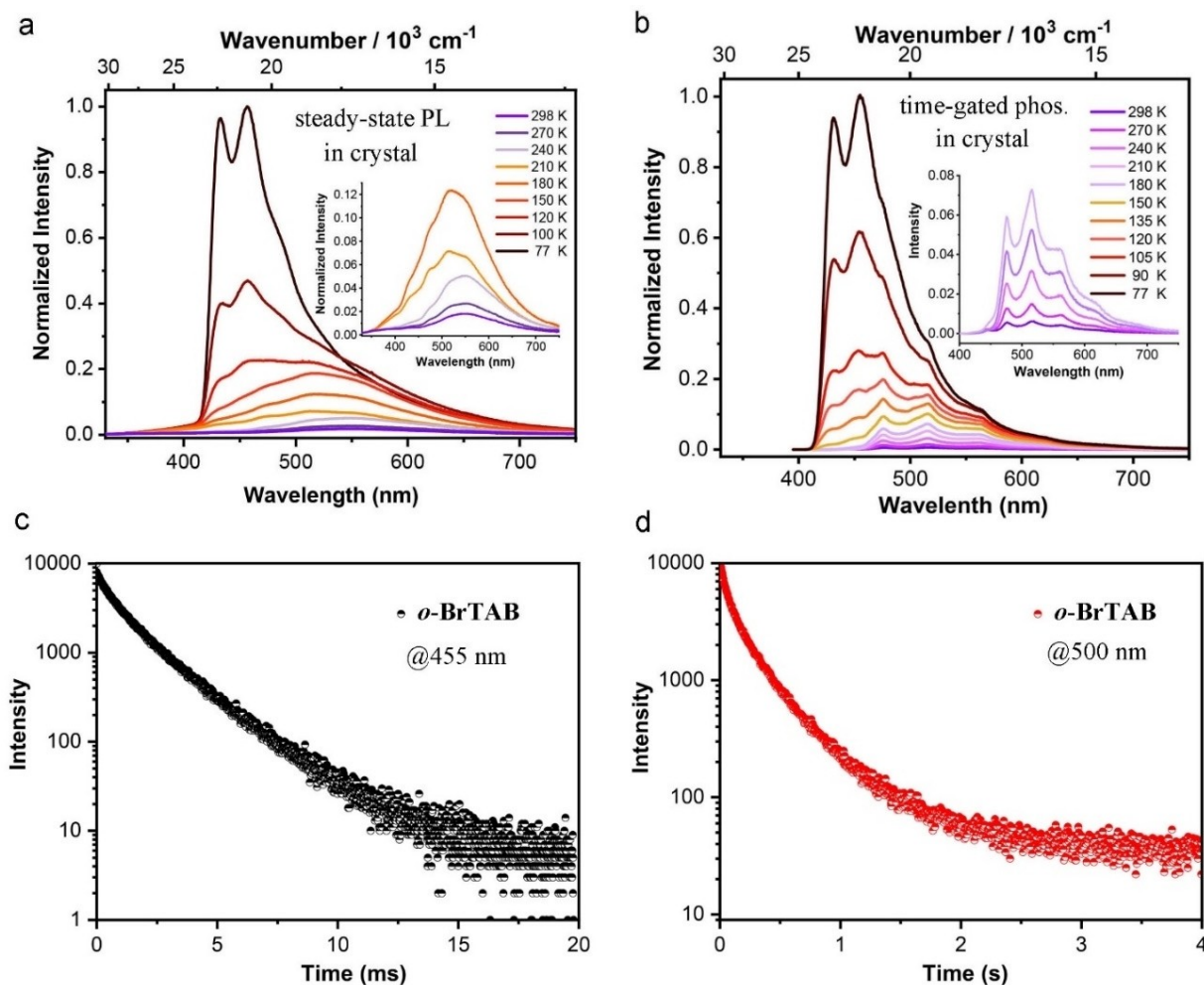


**Figure 7.** (a) Steady-state photoluminescence and (b) time-gated (delay time 0.01 ms) phosphorescence spectra of crystalline *o*-BrTAB at different temperatures ( $\lambda_{\text{ex}} = 305$  nm). Decays of the phosphorescence emission (c) ( $\lambda_{\text{em}} = 455$  nm) and (d) ( $\lambda_{\text{em}} = 500$  nm) of crystalline *o*-BrTAB at 77 K.

substituted aryl ring R1 and the *m*-xylyl group R2 arranged on the opposite side with respect to the Br–C2 bond. Another interesting feature is that the B–C1–C2 angle ( $127.2(2)^\circ$ ) to the C2 carbon atom to which the Br atom is bonded in *o*-BrTAB is significantly larger than all other B–C–C angles in *o*-, *m*- and *p*-BrTAB which are in the range  $117.5(2)$ – $122.9(1)^\circ$  at 100 K (Table S11), and the B–C1–C6 angle ( $117.7(2)^\circ$ ) to the other side of the R1 aryl ring is rather small. The larger B–C1–C2 angle in *o*-BrTAB is attributed to the bulkiness of the long Br–C bond at the *ortho* position of the R1 ring and the Br atom being close to the central B atom and the C atom of the next-nearest *m*-xylyl group R3 with intramolecular Br...B ( $3.345(2)$  Å) and Br...C15 ( $3.298(2)$  Å) distances below the sum of van der Waals radii ( $3.75$  Å for Br...B and  $3.53$  Å for Br...C).<sup>[28]</sup> The effect of the bulkiness of the substituents and, hence, repulsion between methyl groups and also the Br atom, is further observed in the torsion angles between the aryl groups and the BC<sub>3</sub> planes. While the torsion angles are in a similar range ( $50.1$ – $68.6^\circ$ ) for the *m*-xylyl groups, a significantly smaller torsion angle ( $41.9^\circ$ ) is observed for the Br-substituted phenyl rings. Here, the *ortho*-

Br-substituted phenyl ring shows a larger torsion angle ( $38.6(1)^\circ$ ) in *o*-BrTAB than the *meta*- and *para*-Br-substituted phenyl rings ( $20.1$ – $24.8^\circ$ ) in *m*- and *p*-BrTAB due to repulsion effects (Table S11). The molecular geometries in the solid state of *o*-, *m*- and *p*-BrTAB at 290 K, 296 K and 300 K, respectively, are very similar to those at 100 K (Table S12).

The molecules are similarly densely packed in the three compounds as is obvious from the crystal packing coefficients (Table S16). The molecular volumes and molecular surface areas are also very similar. However, the volume of the solvent accessible voids in the unit cells, as calculated with the OLEX2 program,<sup>[29]</sup> is increased in *p*-BrTAB (2.7% at 300 K) and in *m*-BrTAB (4.4% at 296 K) at ambient temperature, compared to *o*-BrTAB (1.7% at 290 K) and to the low-temperature crystal structures at 100 K (0–1.8% in the three compounds). This indicates a looser packing mode in *p*-BrTAB and *m*-BrTAB than in *o*-BrTAB at room temperature.

A Hirshfeld surface analysis based on the crystal structures was performed in order to quantify the nature and type of intermolecular interactions.<sup>[30]</sup> The Hirshfeld surface is a special



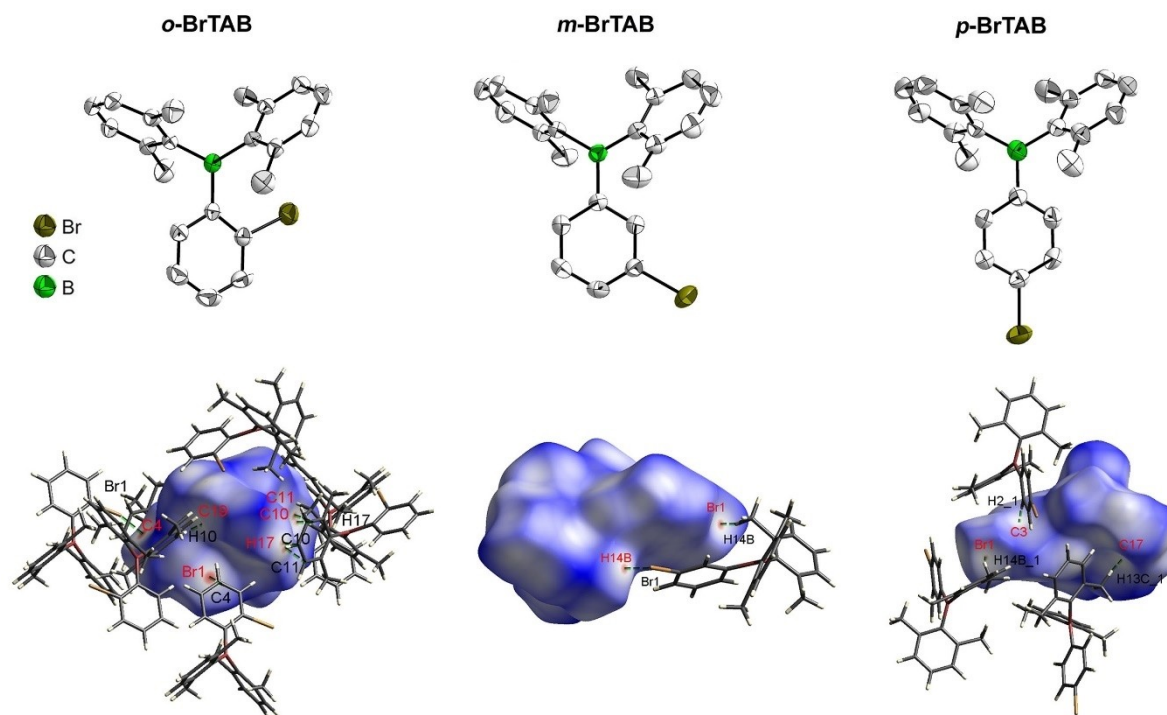


**Figure 8.** The solid-state molecular structure of *o*-BrTAB, *m*-BrTAB and *p*-BrTAB (top left to right) determined by single-crystal X-ray diffraction at room temperature. Ellipsoids are drawn at the 50% probability level, and H atoms are omitted for clarity. Hirshfeld surfaces of *o*-BrTAB, *m*-BrTAB and *p*-BrTAB (bottom left to right) mapped with  $d_{\text{norm}}$  over the range  $-0.12$  to  $1.50$  at room temperature. Neighboring molecules associated with close contacts are shown.

isosurface defined by the weighting function  $w(r)=0.5$  for a particular molecule. This means that the Hirshfeld surface envelops the volume within which the particular molecule contributes more than half of the electron density. Hence, it also includes information on the nearest neighbors and closest contacts to the molecule (Figure 7). The similarity of the amounts and types of interactions in the three compounds is demonstrated in the two-dimensional fingerprint plots and their breakdown to the individual relative contributions (Figures S25 and S26, 100 K).<sup>[31]</sup> At 100 K, major contributions are from H...H interactions (61–67%), followed by a significant amount from C...H (19–25%) and Br...H (10–15%) interactions. Minor contributions (0.2–1.8%) are Br...C, C...C, and Br...Br interactions with C...C interactions being dominant in *m*-BrTAB, Br...Br interactions in one of the symmetry-independent molecules (no. 2) of *p*-BrTAB, and Br...C interactions in both *o*-BrTAB and *p*-BrTAB (Figure S25, Table S16). Relative contributions to intermolecular interactions are very similar for the room temperature structures (Table S16).

At 100 K, the C...H...C interactions are strongest in *o*-BrTAB, with C...H distances in the range 2.735(2)–2.812(2) Å, and two nearly linear interactions with C...H...C = 165.82(15)° and 175.45(15)° (Table S13). C...H...C interactions are weaker in *p*-BrTAB (C...H = 2.810(2)–2.865(2) Å, C...H...C = 131.16(11)–162.62(11)°) although of similar number as in *o*-BrTAB and, significantly, weakest in *m*-BrTAB (C...H = 2.836(2)–2.888(3) Å, C...H...C = 143.96(15)–166.26(15)°) as well as being fewer in number. While there are close Br...H contacts (2.9425(12)–

3.1001(3) Å) in all three compounds, *o*-BrTAB exhibits the closest Br...C contact of 3.354(2) Å. Another close Br...C contact (3.480(2) Å) is found in *p*-BrTAB. In addition, *o*-BrTAB has a short C...C contact (3.361(3) Å) between an aryl ring and a methyl group, and *p*-BrTAB shows two close H...H contacts (2.266 and 2.363 Å) between two aryl rings (Table S16). Interestingly, *m*-BrTAB is the only compound in which two weak intermolecular  $\pi$ ... $\pi$  interactions between aryl rings can be found (Table S15). One involves the Br-substituted phenyl rings with an interplanar separation of 3.640(3) Å and an offset shift of 2.261(4) Å. The nearest-neighbor C...C distance is 3.698(5) Å. The other one involves the R3 xylyl rings with a slightly smaller interplanar separation of 3.544(4) Å, but a larger offset shift of 3.457(4) Å, and a nearest-neighbor C...C distance of 3.637(5) Å.

At room temperature (290 K), there are still a significant number of intermolecular C...H...C interactions (C...H = 2.846(4)–2.873(4) Å, C...H...C = 136.4(2)–177.2(3)°) and a close Br...C contact of 3.432(5) Å present in *o*-BrTAB (Table S13). However, in *m*-BrTAB C...H contacts are long and weak, and the  $\pi$ ... $\pi$  interactions are also insignificant due to large interplanar separations of 3.812(4) Å and 3.645(6) Å with shifts of 2.305(6) Å and 3.437(6) Å, respectively, at 296 K (Table S15). Only a close Br...H interaction (2.9857(8) Å) with a methyl group is still significant. In *p*-BrTAB, two intermolecular C...H...C interactions remain (C...H = 2.870(2) Å and 2.887(2) Å, C...H...C = 145.18(15)° and 132.78(13)°) at 300 K, a close H...H interaction with 2.393(1) Å, and close Br...H interaction (2.9648(4) Å) with a methyl group only (Table S15). Thus, only *o*-

BrTAB exhibits strong intermolecular interactions and, especially, a close Br...C contact at room temperature, which may be the reason that dual phosphorescence is only observed in *o*-BrTAB at room temperature.

In summary, the presence of multiple C—H...C and C—H...Br interactions between molecules in the crystals effectively suppresses the nonradiative decay rate  $k_{nr}$ , which plays an important role in stabilizing the triplet states and achieving RTP. As the strength of intermolecular interactions is especially distinct between the three compounds at room temperature, and is strongest for *o*-BrTAB, this effect may be the reason that we observe DRTP in crystalline *o*-BrTAB at room temperature, but only at low temperature for *m*-BrTAB and *p*-BrTAB.

## Conclusions

We reported three bromo-substituted triarylborane isomers which show persistent room temperature phosphorescence (RTP). Among them, (2-bromophenyl)bis(2,6-dimethylphenyl)borane (*o*-BrTAB) exhibits rare dual room temperature phosphorescence (DRTP) with lifetimes of 0.8 ms (short wavelength component) and 234 ms (long wavelength component), respectively, in the crystalline state. Single-crystal structure analysis shows that multiple molecular C—H...C and C—H...Br contacts in the crystals suppress the nonradiative decay rate  $k_{nr}$  and stabilize the triplet states. In addition, the rigid crystalline matrix provides a favorable environment for realizing dual phosphorescence at room temperature.

## Crystal structures

Deposition Number(s) 2085814 (for *o*-BrTAB at 100 K), 2085815 (for *m*-BrTAB at 100 K), 2085816 (for *p*-BrTAB at 100 K), 2089473 (for *o*-BrTAB at 290 K), 2118234 (for *m*-BrTAB at 296 K) and 2118235 (for *p*-BrTAB at 300 K) contain the supplementary crystallographic data for this paper. These data are provided free of charge by the joint Cambridge Crystallographic Data Centre and Fachinformationszentrum Karlsruhe Access Structures service.

## Acknowledgements

Funding from the Julius-Maximilians-Universität Würzburg and the Deutsche Forschungsgemeinschaft (DFG, German Research Foundation) – GRK2112 and 396890929/GRK 2482 is gratefully acknowledged. We are grateful to the China Scholarship Council for providing a Ph.D. scholarship to Z.W. Open Access funding enabled and organized by Projekt DEAL.

## Conflict of Interest

The authors declare no conflict of interest.

## Data Availability Statement

The data that support the findings of this study are available in the supplementary material of this article.

**Keywords:** AIE · luminescence · phosphorescence · triarylborane · triplet

- [1] a) S. Hirata, K. Totani, J. Zhang, T. Yamashita, H. Kaji, S. R. Marder, T. Watanabe, C. Adachi, *Adv. Funct. Mater.* **2013**, *23*, 3386–3397; b) L. Dou, J. You, Z. Hong, Z. Xu, G. Li, R. A. Street, Y. Yang, *Adv. Mater.* **2013**, *25*, 6642–6671; c) S. Reineke, F. Lindner, G. Schwartz, N. Seidler, K. Walzer, B. Lussem, K. Leo, *Nature* **2009**, *459*, 234–238; d) S. Hirata, K. Totani, H. Kaji, M. Vacha, T. Watanabe, C. Adachi, *Adv. Opt. Mater.* **2013**, *1*, 438–442.
- [2] a) L. Huang, C. Qian, Z. Ma, *Chem. Eur. J.* **2020**, *26*, 11914–11930; b) J. Yang, X. Zhen, B. Wang, X. Gao, Z. Ren, J. Wang, Y. Xie, J. Li, Q. Peng, K. Pu, Z. Li, *Nat. Commun.* **2018**, *9*, 840–849; c) S. Xu, R. Chen, C. Zheng, W. Huang, *Adv. Mater.* **2016**, *28*, 9920–9940; d) J. Zhao, W. Wu, J. Sun, S. Guo, *Chem. Soc. Rev.* **2013**, *42*, 5323–5351; e) H. T. Feng, J. Zeng, P. A. Yin, X. D. Wang, Q. Peng, Z. Zhao, J. W. Y. Lam, B. Z. Tang, *Nat. Commun.* **2020**, *11*, 2617.
- [3] a) Z. He, H. Gao, S. Zhang, S. Zheng, Y. Wang, Z. Zhao, D. Ding, B. Yang, Y. Zhang, W. Z. Yuan, *Adv. Mater.* **2019**, *31*, 1807222; b) T. Maldiney, A. Lecointre, B. Viana, A. Bessiere, M. Bessodes, D. Gourier, C. Richard, D. Scherman, *J. Am. Chem. Soc.* **2011**, *133*, 11810–11815; c) X. F. Wang, H. Y. Xiao, P. Z. Chen, Q. Z. Yang, B. Chen, C. H. Tung, Y. Z. Chen, L. Z. Wu, *J. Am. Chem. Soc.* **2019**, *141*, 5045–5050; d) G. Zhang, G. M. Palmer, M. W. Dewhurst, C. L. Fraser, *Nat. Mater.* **2009**, *8*, 747–751; e) K. Y. Zhang, Q. Yu, H. Wei, S. Liu, Q. Zhao, W. Huang, *Chem. Rev.* **2018**, *118*, 1770–1839.
- [4] a) P. Long, Y. Feng, C. Cao, Y. Li, J. Han, S. Li, C. Peng, Z. Li, W. Feng, *Adv. Funct. Mater.* **2018**, *28*, 1800791; b) Y. Tao, R. Chen, H. Li, J. Yuan, Y. Wan, H. Jiang, C. Chen, Y. Si, C. Zheng, B. Yang, G. Xing, W. Huang, *Adv. Mater.* **2018**, *30*, 1803856; c) B. Zhou, D. P. Yan, *Adv. Funct. Mater.* **2019**, *29*, 1807599.
- [5] a) M. C. Tang, M. Y. Leung, S. L. Lai, M. Ng, M. Y. Chan, V. W. W. Yam, *J. Am. Chem. Soc.* **2018**, *140*, 13115–13124; b) O. S. Wenger, *J. Am. Chem. Soc.* **2018**, *140*, 13522–13533; c) K. Y. Zhang, P. Gao, G. Sun, T. Zhang, X. Li, S. Liu, Q. Zhao, K. K. Lo, W. Huang, *J. Am. Chem. Soc.* **2018**, *140*, 7827–7834; d) W. Liu, J. Wang, Y. Gong, Q. Liao, Q. Dang, Z. Li, B. Liu, *Angew. Chem. Int. Ed.* **2020**, *59*, 20161–20166; *Angew. Chem.* **2020**, *132*, 20336–20341.
- [6] a) C. J. Chen, R. J. Huang, A. S. Batsanov, P. Pander, Y. T. Hsu, Z. G. Chi, F. B. Dias, M. R. Bryce, *Angew. Chem. Int. Ed.* **2018**, *57*, 16407–16411; *Angew. Chem.* **2018**, *130*, 16645–16649; b) L. K. Huang, B. Chen, X. P. Zhang, C. O. Trindle, Y. C. Wang, H. Miao, Y. Luo, G. Q. Zhang, *Angew. Chem. Int. Ed.* **2018**, *57*, 16046–16050; *Angew. Chem.* **2018**, *130*, 16278–16282; c) S. M. A. Fateminia, Z. Mao, S. Xu, Z. Yang, Z. Chi, B. Liu, *Angew. Chem. Int. Ed.* **2017**, *56*, 12160–12164; *Angew. Chem.* **2017**, *129*, 12328–12332; d) K. Jiang, Y. Wang, C. Cai, H. Lin, *Adv. Mater.* **2018**, *30*, 1800783; e) L. Favereau, C. Quinton, C. Poriol, T. Roisnel, D. Jacquemin, J. Crassous, *J. Phys. Chem. Lett.* **2020**, *11*, 6426–6434; f) E. Januszewski, A. Lorbach, R. Grewal, M. Bolte, J. W. Bats, H. W. Lerner, M. Wagner, *Chem. Eur. J.* **2011**, *17*, 12696–12705; g) T. Kushida, C. Camacho, A. Shuto, S. Irlle, M. Muramatsu, T. Katayama, S. Ito, Y. Nagasawa, H. Miyasaka, E. Sakuda, N. Kitamura, Z. Zhou, A. Wakamiya, S. Yamaguchi, *Chem. Sci.* **2014**, *5*, 1296–1304.
- [7] a) J. Wang, Z. Huang, X. Ma, H. Tian, *Angew. Chem. Int. Ed.* **2020**, *59*, 9928–9933; *Angew. Chem.* **2020**, *132*, 10014–10019; b) L. Bian, H. Shi, X. Wang, K. Ling, H. Ma, M. Li, Z. Cheng, C. Ma, S. Cai, Q. Wu, N. Gan, X. Xu, Z. An, W. Huang, *J. Am. Chem. Soc.* **2018**, *140*, 10734–10739; c) W. Zhao, Z. He, B. Z. Tang, *Nature Res. Mater.* **2020**, *5*, 869–885; d) W. Ratzke, L. Schmitt, H. Matsuoka, C. Bannwarth, M. Retegan, S. Bange, P. Klemm, F. Neese, S. Grimme, O. Schiemann, J. M. Lupton, S. Hoger, *J. Phys. Chem. Lett.* **2016**, *7*, 4802–4808; e) E. Lucenti, A. Forni, C. Botta, L. Carlucci, C. Giannini, D. Marinotto, A. Previtali, S. Righetto, E. Cariati, *J. Phys. Chem. Lett.* **2017**, *8*, 1894–1898; f) W. L. Jia, D. T. Song, S. N. Wang, *J. Org. Chem.* **2003**, *68*, 701–705.
- [8] a) M. Louis, H. Thomas, M. Gmelch, A. Haft, F. Fries, S. Reineke, *Adv. Mater.* **2019**, *31*, 1807887; b) H. Shi, Z. An, P. Z. Li, J. Yin, G. Xing, T. He, H. Chen, J. Wang, H. Sun, W. Huang, Y. Zhao, *Cryst. Growth Des.* **2016**, *16*, 808–813; c) H. Tian, X. Ma, C. Xu, J. Wang, *Angew. Chem. Int. Ed.*

- 2018, 57, 10854–10858; *Angew. Chem.* **2018**, 130, 11020–11024; d) J. Wang, C. Wang, Y. Gong, Q. Liao, M. Han, T. Jiang, Q. Dang, Y. Li, Q. Li, Z. Li, *Angew. Chem. Int. Ed.* **2018**, 57, 16821–16826; *Angew. Chem.* **2018**, 130, 17063–17068; e) Z. Y. Zhang, Y. Chen, Y. Liu, *Angew. Chem. Int. Ed.* **2019**, 58, 6028–6032; *Angew. Chem.* **2019**, 131, 6089–6093; f) J. L. Ma, H. Liu, S. Y. Li, Z. Y. Li, H. Y. Zhang, Y. Wang, C. H. Zhao, *Organometallics* **2020**, 39, 4153–4158; g) J. Gierschner, J. Shi, D. Roca-Sanjuán, B. Milián-Medina, S. Varghese, S. Y. Park, *Adv. Opt. Mater.* **2021**, 2002251; h) H. Yuasa, S. Kuno, *Bull. Chem. Soc. Jpn.* **2018**, 91, 223–229.
- [9] a) R. Kabe, C. Adachi, *Nature* **2017**, 550, 384–387; b) D. Li, F. Lu, J. Wang, W. Hu, X. M. Cao, X. Ma, H. Tian, *J. Am. Chem. Soc.* **2018**, 140, 1916–1923; c) J. Wei, B. Liang, R. Duan, Z. Cheng, C. Li, T. Zhou, Y. Yi, Y. Wang, *Angew. Chem. Int. Ed.* **2016**, 55, 15589–15593; *Angew. Chem.* **2016**, 128, 15818–15822; d) Z. Lin, R. Kabe, K. Wang, C. Adachi, *Nat. Commun.* **2020**, 11, 191; e) B. Chen, W. Huang, H. Su, H. Miao, X. Zhang, G. Zhang, *Angew. Chem. Int. Ed.* **2020**, 59, 10023–10026; *Angew. Chem.* **2020**, 132, 10109–10112; f) O. Bolton, K. Lee, H. J. Kim, K. Y. Lin, J. Kim, *Nat. Chem.* **2011**, 3, 205–210; g) C. Chen, Z. Chi, K. C. Chong, A. S. Batsanov, Z. Yang, Z. Mao, Z. Yang, B. Liu, *Nat. Mater.* **2020**, 20, 175–180.
- [10] a) Y. Gong, G. Chen, Q. Peng, W. Z. Yuan, Y. Xie, S. Li, Y. Zhang, B. Z. Tang, *Adv. Mater.* **2015**, 27, 6195–6201; b) Y. Gong, L. Zhao, Q. Peng, D. Fan, W. Z. Yuan, Y. Zhang, B. Z. Tang, *Chem. Sci.* **2015**, 6, 4438–4444; c) D. C. Green, M. A. Holden, M. A. Levenstein, S. Zhang, B. R. G. Johnson, J. Gala de Pablo, A. Ward, S. W. Botchway, F. C. Meldrum, *Nat. Commun.* **2019**, 10, 206; d) K. Narushima, Y. Kiyota, T. Mori, S. Hirata, M. Vacha, *Adv. Mater.* **2019**, 31, 1807268.
- [11] a) Q. Li, M. Zhou, M. Yang, Q. Yang, Z. Zhang, J. Shi, *Nat. Commun.* **2018**, 9, 734; b) H. W. Wu, W. J. Chi, Z. Chen, A. K. Bindra, G. B. Yang, X. G. Liu, Y. L. Zhao, *Adv. Funct. Mater.* **2019**, 29, 1807243; c) A. D. Nidhankar, Goudappagouda, D. S. Mohana Kumari, S. K. Chaubey, R. Nayak, R. G. Gonnade, G. V. P. Kumar, R. Krishnan, S. S. Babu, *Angew. Chem. Int. Ed.* **2020**, 59, 13079–13085; *Angew. Chem.* **2020**, 132, 13179–13185.
- [12] a) Z. Chai, C. Wang, J. Wang, F. Liu, Y. Xie, Y. Z. Zhang, J. R. Li, Q. Li, Z. Li, *Chem. Sci.* **2017**, 8, 8336–8344; b) X. F. Chen, C. Xu, T. Wang, C. Zhou, X. P. Zhang, J. N. Demas, C. O. Trindle, G. Q. Zhang, *Angew. Chem. Int. Ed.* **2016**, 55, 9872–9876; *Angew. Chem.* **2016**, 128, 10026–10030; c) P. K. Samanta, D. Kim, V. Coropceanu, J. L. Bredas, *J. Am. Chem. Soc.* **2017**, 139, 4042–4051; d) Y. Shoji, Y. Iwabata, Q. Wang, D. Nemoto, A. Sakamoto, N. Tanaka, J. Seino, H. Nakai, T. Fukushima, *J. Am. Chem. Soc.* **2017**, 139, 2728–2733; e) J. Yang, X. Gao, Z. Xie, Y. Gong, M. Fang, Q. Peng, Z. Chi, Z. Li, *Angew. Chem. Int. Ed.* **2017**, 56, 15299–15303; *Angew. Chem.* **2017**, 129, 15501–15505; f) E. Hamzehpoor, D. F. Perepichka, *Angew. Chem. Int. Ed.* **2016**, 59, 9977–9981; *Angew. Chem.* **2016**, 132, 10063–10067.
- [13] a) S. A. Bagnicha, N. N. Khropika, V. N. Krykshoia, A. L. Mikhalchuk, *Chem. Phys.* **2001**, 274, 29–35; b) S. Bhattacharyya, L. R. Sousa, S. Ghosh, *Chem. Phys. Lett.* **1997**, 269, 314–320; c) T. Itoh, *J. Chem. Phys.* **1987**, 87, 4361–4367; d) T. Itoh, *J. Lumin.* **2004**, 109, 221–225; e) T. Nakayama, K. Sakurai, K. Ushida, K. Kawatsura, K. Hamaou, *Chem. Phys. Lett.* **1989**, 164, 557–561; f) S. Samanta, M. B. Roy, M. Chatterjee, S. Ghosh, *J. Lumin.* **2007**, 126, 230–238.
- [14] Z. He, W. Zhao, J. W. Y. Lam, Q. Peng, H. Ma, G. Liang, Z. Shuai, B. Z. Tang, *Nat. Commun.* **2017**, 8, 416.
- [15] F. Y. Li, S. Guo, Y. Y. Qin, Y. X. Shi, M. P. Han, Z. F. An, S. J. Liu, Q. Zhao, W. Huang, *Adv. Opt. Mater.* **2019**, 7, 1900511.
- [16] T. Wang, Z. B. Hu, X. C. Nie, L. K. Huang, M. Hui, X. Sun, G. Q. Zhang, *Nat. Commun.* **2021**, 12, 1364.
- [17] Y. Liu, Z. M. Ma, J. W. Liu, M. X. Chen, Z. Y. Ma, X. R. Jia, *Adv. Opt. Mater.* **2021**, 9, 2001685.
- [18] a) S. J. Woo, Y. H. Kim, J. J. Kim, *Chem. Mater.* **2021**, 33, 5618–5630; b) T. Wang, X. G. Su, X. P. Zhang, X. C. Nie, L. K. Huang, X. Y. Zhang, X. Sun, Y. Luo, G. Q. Zhang, *Adv. Mater.* **2019**, 31, 1904273; c) C. Zhou, S. Zhang, Y. Gao, H. Liu, T. Shan, X. Liang, B. Yang, Y. Ma, *Adv. Funct. Mater.* **2018**, 28, 1802407; d) S. K. Behera, S. Y. Park, J. Gierschner, *Angew. Chem. Int. Ed.* **2021**, 60, 22624–22638; *Angew. Chem.* **2021**, 133, 22804–22820.
- [19] a) A. Fukazawa, S. Yamaguchi, *Chem. Asian J.* **2009**, 4, 1386–1400; b) X. Wang, S. L. Gong, D. T. Song, Z. H. Lu, S. N. Wang, *Adv. Funct. Mater.* **2014**, 24, 7257–7271; c) M. Hirai, N. Tanaka, M. Sakai, S. Yamaguchi, *Chem. Rev.* **2019**, 119, 8291–8331; d) Z. M. Hudson, S. N. Wang, *Acc. Chem. Res.* **2009**, 42, 1584–1596; e) S. Yamaguchi, A. Wakamiya, *Pure Appl. Chem.* **2006**, 78, 1413–1424; f) F. Jäkle, *Chem. Rev.* **2010**, 110, 3985–4022; g) E. Grotthuss, A. John, T. Kaese, M. Wagner, *Asian J. Org. Chem.* **2018**, 7, 37–53; h) R. J. Kahan, W. Hirunpinyopas, J. Cid, M. J. Ingleson, R. A. W. Dryfe, *Chem. Mater.* **2019**, 31, 1891–1898; i) S. S. Kothavale, J. Y. Lee, *Adv. Opt. Mater.* **2020**, 8, 2000922; j) M. Gon, K. Tanaka, Y. Chujo, *Bull. Chem. Soc. Jpn.* **2019**, 92, 7–18; k) G. Turkoglu, M. E. Cinar, T. Ozturk, *Molecules* **2017**, 22, 1522; l) H. H. Hackney, D. F. Perepichka, *Aggregate* **2021**, e123; m) H. E. Hackney, D. G. Hall, *Chem-PhotoChem* **2022**, e202100219.
- [20] a) Z. Yuan, N. J. Taylor, T. B. Marder, I. D. Williams, S. K. Kurtz, L.-T. Cheng, *J. Chem. Soc. Chem. Commun.* **1990**, 1489–1492; b) C. D. Entwistle, T. B. Marder, *Angew. Chem. Int. Ed.* **2002**, 41, 2927–2931; *Angew. Chem.* **2002**, 114, 3051–3056; c) C. D. Entwistle, T. B. Marder, *Chem. Mater.* **2004**, 16, 4574–4585; d) L. Ji, S. Griesbeck, T. B. Marder, *Chem. Sci.* **2017**, 8, 846–863; e) J. He, F. Rauch, M. Finze, T. B. Marder, *Chem. Sci.* **2021**, 12, 128–147; f) S. M. Berger, T. B. Marder, *Mater. Horiz.* **2022**, 9, 112–120; g) Z. Wu, J. C. Roldao, F. Rauch, A. Friedrich, M. Ferger, F. Würthner, J. Gierschner, T. B. Marder, *Angew. Chem. Int. Ed.* **2022**, 61, e202200599; *Angew. Chem.* **2022**, 134, e202200599.
- [21] a) Z. Wu, J. Nitsch, J. Schuster, A. Friedrich, K. Edkins, M. Loebnitz, F. Dinkelbach, V. Stepanenko, F. Würthner, C. M. Marian, L. Ji, T. B. Marder, *Angew. Chem. Int. Ed.* **2020**, 59, 17137–17144; *Angew. Chem.* **2020**, 132, 17285–17292; b) Z. Wu, J. Nitsch, T. B. Marder, *Adv. Opt. Mater.* **2021**, 2100411.
- [22] a) Q. Peng, H. Ma, Z. Shuai, *Acc. Chem. Res.* **2021**, 54, 940–949; b) A. D. Nidhankar, Goudappagouda, V. C. Wakchaure, S. S. Babu, *Chem. Sci.* **2021**, 12, 4216–4236.
- [23] a) V. Stehr, R. F. Fink, B. Engels, J. Pflaum, C. Deibel, *J. Chem. Theory Comput.* **2014**, 10, 1242–1255; b) M. Tabachnyk, B. Ehrler, S. Bayliss, R. H. Friend, N. C. Greenham, *Appl. Phys. Lett.* **2013**, 103, 153302.
- [24] S. M. Berger, M. Ferger, F. Rauch, T. B. Marder, *Chem. Eur. J.* **2021**, 27, 9094–9101.
- [25] S. Sarkar, H. P. Hendrickson, D. Lee, F. Devine, J. Jung, E. Geva, J. Kim, B. D. Dunietz, *J. Phys. Chem. C* **2017**, 121, 3771–3777.
- [26] C. M. Marian, Spin-Orbit Coupling in Molecules. In Reviews in Computational Chemistry (eds K. B. Lipkowitz, D. B. Boyd), **2001**. <https://doi.org/10.1002/0471224413.ch3>.
- [27] a) M. A. El-Sayed, *Acc. Chem. Res.* **1968**, 1, 8–16; b) C. M. Marian, *Annu. Rev. Phys. Chem.* **2021**, 72, 617–640.
- [28] M. Mantina, A. C. Chamberlin, R. Valero, C. J. Cramer, D. G. Truhlar, *J. Phys. Chem. A* **2009**, 113, 5806–5812.
- [29] O. V. Dolomanov, L. J. Bourhis, R. J. Gildea, J. A. K. Howard, H. Puschmann, *J. Appl. Crystallogr.* **2009**, 42, 339–341.
- [30] a) J. J. McKinnon, A. S. Mitchell, M. A. Spackman, *Chem. Eur. J.* **1998**, 4, 2136–2141; b) J. J. McKinnon, M. A. Spackman, A. S. Mitchell, *Acta Crystallogr. Sect. B* **2004**, 60, 627–668; c) M. A. Spackman, P. G. Byrom, *Chem. Phys. Lett.* **1997**, 267, 215–220; d) M. A. Spackman, D. Jayatilaka, *CrystEngComm* **2009**, 11, 19–32.
- [31] a) J. J. McKinnon, D. Jayatilaka, M. A. Spackman, *Chem. Commun.* **2007**, 3814–3816; b) A. Parkin, G. Barr, W. Dong, C. J. Gilmore, D. Jayatilaka, J. J. McKinnon, M. A. Spackman, C. C. Wilson, *CrystEngComm* **2007**, 9, 648–652; c) M. A. Spackman, J. J. McKinnon, *CrystEngComm* **2002**, 4, 378–392.

Manuscript received: February 17, 2022

Accepted manuscript online: March 24, 2022

Version of record online: April 8, 2022